ABSTRACT

Performance of the Prototype Readout System for the CMS Endcap Hadron Calorimeter Upgrade

Nathaniel Chaverin

Director: Jay Dittmann, Ph.D.

The Compact Muon Solenoid (CMS) experiment at the CERN Large Hadron Collider (LHC) will upgrade the photodetectors and readout systems of the endcap hadron calorimeter during the technical stop scheduled for late 2016 and early 2017. A major milestone for this project was a highly successful test beam run at CERN in August 2015. The test beam run served as a full integration test of the electronics, allowing a study of the response of the preproduction electronics to the true detector light profile, as well as a test of the light yield of various new plastic scintillator materials. We present implications for the performance of the hadron calorimeter front-end electronics based on test beam data.

APPROVED BY DIRECTOR OF HONORS THESIS:

_____

Dr. Jay Dittmann, Department of Physics

APPROVED BY THE HONORS PROGRAM:

_____

Dr. Andrew Wisely, Director

DATE: _____

# PERFORMANCE OF THE PROTOTYPE READOUT SYSTEM FOR THE CMS ENDCAP HADRON CALORIMETER UPGRADE

A Thesis Submitted to the Faculty of

Baylor University

In Partial Fulfillment of the Requirements for the

Honors Program

By

Nathaniel Chaverin

Waco, Texas

April 2016

TABLE OF CONTENTS

LIST OF FIGURES

LIST OF TABLES

# ACKNOWLEDGMENTS

I would like to extend my thanks to the entire Baylor physics department, especially the members of the High Energy Physics research group, for their guidance and support throughout my research experience. In particular, I would like to thank Dr. Jay Dittmann, my advisor and thesis mentor, who has dedicated much of his time and energy to fostering my research and academics, and without whose expertise and advice this thesis would not have been possible. I would like to extend special thanks to Dr. Kenichi Hatakeyama, who taught my first Baylor physics class and gave me my first opportunity to engage in physics research. Thanks as well to Drs. Nathaniel Pastika and Nadja Strobbe, who also taught me a great deal about research and the life of a researcher. I am further indebted to Drs. Zhenrong Zhang and Walter Wilcox for agreeing to be readers for my thesis and suggesting their improvements. I would also like to extend a special word of thanks to Dr. Dennis A. Johnston of the Baylor Statistics Department, who graciously and spontaneously provided monetary support to allow me to have the opportunity to go to CERN to be a part of this research.

Lastly, I would like to acknowledge the support of the United States Department of Energy, which continues to provide funding for CMS and many other experiments in particle physics.

# CHAPTER ONE

## Overview of Particle Physics and High Energy Physics Research

### *1.1 Introduction*

Ever since the days of the Greek scholars who divided the physical world into water, earth, air, and fire, the cutting edge of scientific thought has concerned itself with the question of substance: what are we all made of? Like a child taking apart a watch, scientists and natural philosophers throughout history have studied the origins of matter out of a shared curiosity about the nature of things. In the intervening time, this question has been answered many times, with greater and greater accuracy. From Democritus, who first postulated the existence of fundamental particles, to Mendeleev, who first assembled the periodic table of elements, the search for elegance in the universe has led thinkers toward theories that explain a large amount of complexity with the simplest possible explanation. Fundamental to this paradigm is the principle that the universe is inherently ordered, structured, and comprehensible—a belief that has so far led to many advances in our understanding of our surroundings.

Particle physics extends this principle to the subatomic scale, providing an explanation for the interactions of bits of matter too small even to be directly detected. Throughout the last several centuries, achievements in the field continued to push the limit of the size of phenomena that could be understood. Starting with Dalton and Avogadro's formalization of atomic theory in the 19$^{th}$ century, evidence gradually accumulated that matter was not a continuous substance, but rather was composed of

discrete particles of finite size. Like many of today's advances, this process of understanding was motivated partially by theory and partially by experiment, as the then-novel idea of atoms proved to be an excellent description of many thermodynamic systems. Gradually, the scientific community came to understand that many different phenomena could be understood in terms of the interactions of tiny pieces of matter.

As the tools of the trade became more precise, particles even smaller than atoms were discovered: the electron in 1897, the proton in 1920, and many more in the following years. Throughout the 20$^{th}$ century, particle detectors expanded the list of known subatomic particles into a "zoo" of exotic species (see Section 1.1). Eventually, the discipline hit a limitation on the mass of particles that it could examine from natural phenomena. To get around this natural bound on particle mass, the idea of a particle accelerator—a device for accelerating and colliding particles to produce new particles—was introduced in the 1930's. The experimentalists of the time found that the higher the energy of the colliding bits of matter, the smaller the length scales that could be probed, much like shooting a BB gun through a peach to find the shape of its pit [1, 2].

The evolution of accelerators culminated in the 2009 inauguration of the world's largest particle accelerator, the Large Hadron Collider (LHC) at the European Organization for Nuclear Research (CERN). Capable of accelerating two opposing proton beams to very nearly the speed of light, it has allowed tremendous insight into extremely fundamental phenomena. Central to its operation are several detectors which measure the products of the colliding protons. These are maintained and controlled by collaborations of scientists, engineers, and technicians, often numbering in the thousands. Two of these detectors, the Compact Muon Solenoid (CMS) and A Toroidal LHC

ApparatuS (ATLAS), announced in 2012 the discovery of the Higgs Boson, an elementary particle that had eluded scientific discovery for nearly 50 years.

In order to continue its record of success, the LHC undergoes periodic shutdowns every several years for purposes of maintenance and improvement. One such shutdown, the 2016–17 Extended Year-End Technical Stop (EYETS 2016-17), is slated to occur beginning in December 2016. During this time, the LHC, as well as the particle detectors, will be repaired and upgraded. As part of the planning process for EYETS 2016–17, the CMS collaboration created plans for a number of major improvements to the hardware of the CMS detector, and has been testing them to prepare for their inclusion in the improved future configuration. The subject of this thesis is a number of such hardware tests which took place in summer 2015 at CERN. Following a general introduction to particle physics, the following chapters of this thesis will describe the nature of these upgrades in detail and present our results from our testing of certain next-generation hardware components and systems [3].

### *1.2 The Standard Model*

The product of decades of theoretical and experimental work, the Standard Model is one of the most successful theories of all time. It is the fundamental particle analogue of the periodic table of elements, representing all known particles that cannot be rendered into smaller components. Without distinguishing between particles and their corresponding antiparticles and among the many color states of quarks and gluons, the Standard Model consists of 17 particles—the "elements" of subatomic physics. Twelve of the particles ("fermions") comprise matter, although only three of them make up all of

the “normal” matter in the universe. The remaining five (“bosons”) govern forces. The fermions are further subdivided into two classes: quarks, which combine to create the LHC’s eponymous hadrons, and leptons.

While it is common knowledge that atoms are made up of protons, neutrons, and electrons, it is perhaps less well known that the protons and neutrons that compose each atom’s nucleus are themselves made up of smaller entities known as quarks (see Table 1.1). There are six types, or “flavors,” of quark, along with their respective antiparticles, which have the same mass but opposite electric charge. Quarks are governed not only by the electromagnetic force, responsible for electrical attraction and repulsion, but also the strong force, a short-ranged but extremely powerful force responsible for keeping them tightly bound to at least one partner at all times. This property causes them to form bound combinations of two or three known as hadrons. Two-quark hadrons are termed “mesons,” from the Greek word *mesos*, meaning intermediate, and three-quark hadrons are called “baryons,” from the Greek *barys*, meaning heavy. The proton and neutron are both examples of baryons; the proton consists of two up quarks and a down quark, while the neutron consists of two down quarks and an up quark. Quarks come in three “colors,” red, green, and blue (with anti-red, anti-green and anti-blue for an antiquark); the total color of a hadron is required to be “white” (red + green + blue, or color + anti-color).

| First Generation | Second Generation | Third Generation |
|---|---|---|
| Up quark (u) | Charm quark (c) | Top quark (t) |
| Down quark (d) | Strange quark (s) | Bottom quark (b) |

*Table 1.1:* The quarks.

The remainder of the fermions are the six leptons (see Table 1.2). Three of these are neutrinos, ghostly neutral particles with very little mass, which pass very easily through matter. The other three are the electron and its two cousins, the muon and the tau (together, again, with their corresponding antiparticles). Each neutrino is associated with one of the other leptons, resulting in the electron neutrino, the muon neutrino, and the tau neutrino. Because of their very weak interaction with matter, they can be very hard to detect.

| First Generation | Second Generation | Third Generation |
|---|---|---|
| Electron (e) | Muon (μ) | Tau (τ) |
| Electron neutrino ($\nu_e$) | Muon neutrino ($\nu_\mu$) | Tau neutrino ($\nu_\tau$) |

*Table 1.2:* The leptons.

Between them, the up quark, down quark, and electron comprise all of the visible matter in the universe. Since the up and down quarks make up protons and neutrons, which in combination with electrons make up atoms, atomic matter—everything made of atoms—is, at the base level, composed of just three different fundamental particles. The question of why there are so many other fundamental fermions is a legitimate one, and it is the subject of ongoing research.

Besides the 12 matter particles, there are also five other particles, called gauge bosons (Table 1.3). Four of them regulate fundamental forces, whereas the fifth, the recently discovered Higgs, is responsible for fundamental particles having mass. The four force carriers are each associated with a fundamental force of nature. The photon is the massless mediator of the electromagnetic force. This force is responsible for both electric and magnetic phenomena. It also governs light, which can be thought of as a wave of

intermingled magnetic and electric fields. Along with gravity, this force is by far the most familiar to us, as it is the reason why objects are solid, as well as why atoms can form at all, since it causes negatively-charged electrons to bind to positively-charged atomic nuclei.

The gluon, also massless, is the carrier for the previously mentioned strong force, which binds together quarks, as well as protons and neutrons in atomic nuclei. The most powerful force in nature, the strong force only works over extremely short distances, usually less than the width of a proton. Unlike that of more familiar forces such as gravity or electromagnetism, the effect of the strong force increases with distance; the more separated two bound quarks become, the more they attract each other. If they are pulled apart with sufficient force, the energy stored in the attraction between them can become so great as to create new particles, according to Einstein's theory of the interchangeability of mass and energy. Thus, if two hadrons collide with sufficient energy, the result can be a cascade of new particles, called a "jet." These structures are often seen in detectors such as CMS, and are a key component of many analyses.

| Particle (Symbol) | Effect |
|---|---|
| Photon ($\gamma$) | Electromagnetic force |
| Gluon (g) | Strong nuclear force |
| W boson ($W^+$ and $W^-$) | Weak nuclear force |
| Z boson ($Z^0$) | Weak nuclear force |
| Higgs boson (H) | Gives particles mass |

*Table 1.3:* The gauge bosons

The W and Z bosons are responsible for the so-called weak force, which is the mechanism by which one particle can decay into another particle—a very important

property in the world of collider physics, as will be shown. A fifth force particle, the graviton, is thought to regulate gravity, but it has not been conclusively shown to exist. Rather, gravity is described by Einstein's theory of general relativity, which deals with large length scales. Unifying the theory of relativity with the theory of quantum mechanics, which is responsible for the behavior of subatomic particles, is one of the most prominent goals of modern-day theoretical physics.

Together, this set of fundamental particles makes up the "elements" of subatomic physics [4].

The purpose of detectors such as those associated with the LHC is to observe interactions involving these elementary particles, understand the processes by which they were produced, and compare the results to current theory in the hopes of finding new discoveries in physics.

# CHAPTER TWO

## Motivation: The LHC, CMS, and Upgrades

### *2.1 Physical Processes in the LHC*

In order to facilitate an understanding of the goals and methods of the research that led to this thesis, it is necessary to provide a brief outline of the physical principles that govern the day-to-day operation of a particle accelerator like the Large Hadron Collider and its associated experiments. Two important physical phenomena that are vital to the operation of the LHC are a) relativistic effects and b) scintillation. A short summary of each effect follows.

#### *2.1.1 Brief Introduction to Special Relativity*

Conceived in 1905 by Albert Einstein, the Special Theory of Relativity was constructed in part as an explanation for certain unintuitive findings in Maxwell's formalization of electromagnetic theory. Of particular importance was the seemingly paradoxical result that the speed of light, which itself is an electromagnetic wave, should appear to all observers to have the same constant value, regardless of location, speed, or direction—roughly $3.00 \times 10^8$ meters per second. Whereas previous theorists had attempted to explain this in terms of the increasingly strained Luminiferous Ether Theory of the time, Einstein took the conclusion at face value, constructing a formalism in which the speed of light was invariant, but variables such as length and time were not. This

resolved many of the apparent paradoxes associated with Maxwell's results, and a fuller treatment was provided in 1915's General Theory of Relativity.

Einstein's theory leads to a number of effects that are very relevant to the world of high energy physics research. Because modern accelerators can impart large energies to subatomic particles, they cause them to move at speeds extremely close to the speed of light. Protons in the Large Hadron Collider move only a few meters per second slower than light; in this regime, relativistic effects are very prominent. Thus, it is important to understand what to expect when observing a particle moving at such speeds.

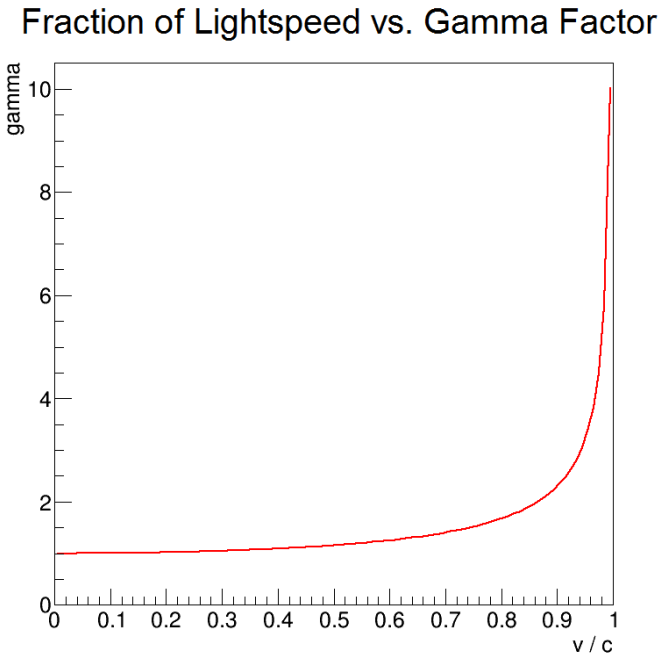


Figure 2.1: Fraction of lightspeed vs. gamma factor. The factor governing relativistic effects asymptotically approaches infinity near $v/c = 1$.

First, an object with relativistic velocity will experience time dilation. This effect causes outside observers to conclude that the "clock" of the object has slowed down. For example, when high energy subatomic particles from space collide with atoms in the upper atmosphere, they can produce particles known as muons (more on these later).

These muons are known to have a very short lifetime and will decay very quickly, becoming other particles. This process takes place so rapidly, in fact, that relativity is needed to explain the large number of muons that can be detected making it from the top of the atmosphere to the surface of the earth. Without such effects, the lifetime of the muon is sufficiently short as to cause most of the particles to decay before reaching the earth's surface. However, because they are moving at speeds very close to that of light, observers in the earth's frame of reference measure the time it takes for a muon to decay becoming dilated, meaning that they have "more time" to make it to detectors at sea level. This effect is governed by the so called "gamma factor," which is given by

$$\gamma = \frac{1}{\sqrt{1 - \left(\frac{v}{c}\right)^2}}$$

where $\gamma$ is the gamma factor, $v$ is the speed of the object, and $c$ is the speed of light in a vacuum. This factor, which governs many of the effects of relativity, becomes asymptotically large at velocities close to light (see Fig. 2.1).

The second prominent effect of relativity is that of mass-energy equivalence. Described by Einstein's famous equation $E = mc^2$, this aspect of the theory states that mass and energy are fundamentally related, and that one can be turned into the other. In this formula, the term $c^2$, where c is the speed of light in a vacuum, acts as a "conversion rate" between mass and energy. Because the speed of light is large, it follows that even a small amount of mass is equivalent to a large amount of energy. As an example, the conversion of a single gram of mass into energy would produce

$$E = mc^2 = (1.00 \times 10^{-3}\ \text{kg})\left(3.00 \times 10^8 \frac{\text{m}}{\text{s}}\right)^2 = 9.00 \times 10^{13}\ \frac{\text{kg} \cdot \text{m}^2}{\text{s}^2}$$

$$= 9.00 \times 10^{13}\ \text{J}$$

of energy, or 90 terajoules (90 trillion joules). For perspective, this is roughly as much energy as the Hoover Dam produces in 12 hours of normal operation. This tremendous conversion factor is the source of the impressive power that can be produced by nuclear power stations, which indirectly rely on this effect. Conversely, energy has an associated mass, so that a stretched spring weighs imperceptibly more than an equivalent un-stretched one. Likewise, a very energetic particle will be measured to have more "mass" than an equivalent particle at a lower energy.

This ties directly into the related phenomenon of so-called "relativistic mass." Although a massive particle's speed is constrained to be slower than the speed of light, its kinetic energy (energy associated with its motion) is not constrained, and will keep increasing the more the particle is "pushed." Thus, near light-speed, a difference in speed of a meter per second might impart hundreds of times more energy into the particle. Because of mass-energy equivalence, the particle can be thought of as having a large "relativistic mass," which is governed by the aforementioned gamma factor [5].

One major result of these effects is that when two relativistic protons collide in the LHC, their combined apparent mass is much larger than it would be if they were stationary. Thus, when the collision occurs, the total mass of the produced particles far exceeds that of two protons at rest. Because of this effect, researchers in high energy physics often forgo describing the exact speed of a particle, opting instead to refer to its energy, which is often given in units of electron volts (eV). One eV is equal to the amount of energy needed to move one electron through a potential difference of one volt. The current energy of each proton in the LHC is approximately 6.5 TeV, or 6.5 trillion eV. When two protons collide, the energy of the collision is measured in terms of the

center of mass energy, or the energy recorded in the frame of reference of the detector. In this frame, the total energy of such head-on collisions is simply the sum of the energies of the two particles; thus the collision energy of the LHC is said to be approximately 13 TeV [6].

### *2.1.2 Brief Introduction to Scintillation*

After high energy particles are produced in LHC collisions, they travel outward from the beamline until they enter the volume of a detector. Some of these particles are leptons, some are hadrons. In the case of CMS, the hadronic component of the collision products is measured by the Hadron Calorimeter, which detects particles using the phenomenon of scintillation. This is the process by which the energy of a subatomic particle is converted to light inside specially-doped plastic scintillator materials. In CMS, these materials are used in the form of flat "tiles," which are stacked into towers and used to gain information about both particle location and timing. Each time a particle deposits its energy in one such tile in CMS, the light from the exposure is carried by fiber-optic cables to be detected by sensitive electronics. It is these electronics, divided into the "front-end" and "back-end" electronics, that were the focus of the 2015 test beam.

## *2.2 Overview of the Large Hadron Collider*

The Large Hadron Collider (LHC) is currently the highest-energy particle collider in the world. Located in Geneva, Switzerland, it is sufficiently large that it straddles the border between Switzerland and France. Proton beams are produced in smaller accelerators, then passed through a series of upward steps in energy until they are

injected into the LHC itself. The main body of the LHC consists of an underground ring 27 kilometers in circumference, in which superconducting magnets guide bunches of protons in two counter-rotating paths, one atop the other. These proton bunches are then guided to collide with one another in special detector halls. As noted above, the tremendous amount of kinetic energy in the protons as they collide creates a highly diverse shower of particles. These products are measured by specially-designed multi-layer detectors such as ATLAS, CMS, ALICE, and LHCb (Figure 2.2).

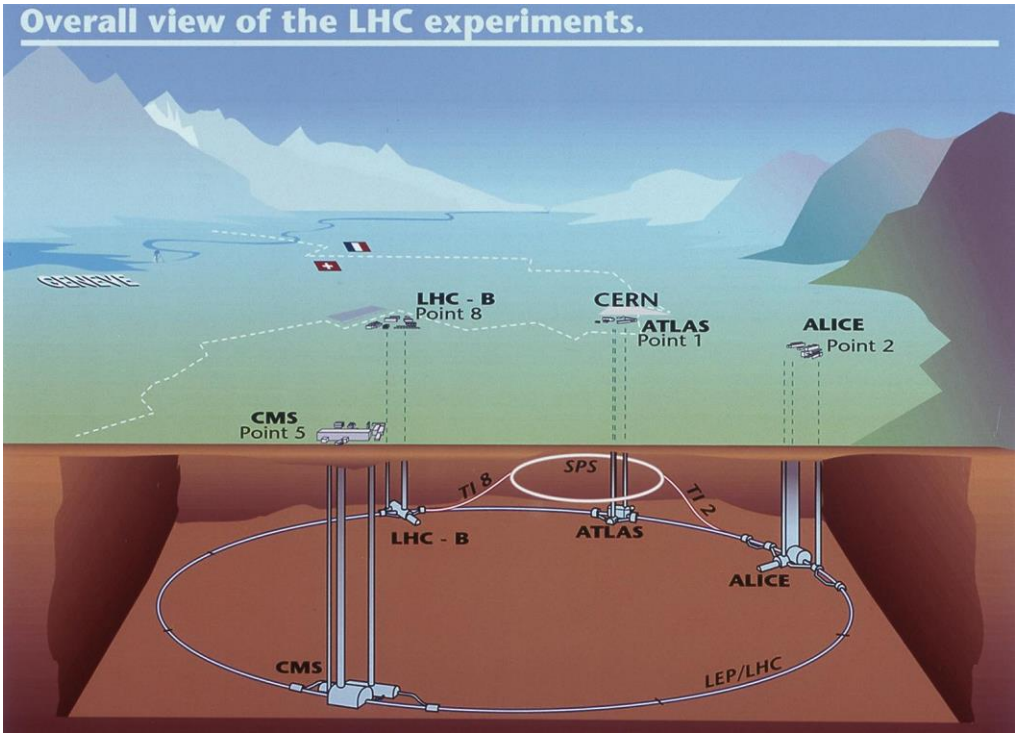

Figure 2.2: The Large Hadron Collider and associated experiments. Protons begin at CERN and are accelerated in a series of steps before injection into the main ring [7].

Each of these detectors is tuned for its stated function; ATLAS and CMS are designed to capture the full range of particles produced, to facilitate multi-faceted and diverse analyses, whereas LHCb and ALICE are more specialized in their focus. The ATLAS and CMS collaborations, because they are comparable in scope and number of

researchers, are able to interact and cross-check one another's results, leading to a productive interplay between the two. This thesis was completed as part of the CMS experiment.

### *2.2.1 The LHC Accelerator Chain*

The proton bunches used in the LHC, although they are destined to reach energies of nearly 7 TeV, begin their journey at much more prosaic energy levels. The ultimate source of protons for the experiments is a bottle of hydrogen gas in the Linear Accelerator 2 (Linac 2) facility in the CERN Meyrin site. Hydrogen atoms, which consist of a single electron orbiting a proton, make ideal proton sources once the electrons have been stripped off by a strong electric field. The resulting proton beam is then placed in the aforementioned Linear Accelerator, which gives them a large velocity using oscillating electric fields. These are provided by radiofrequency (RF) cavities, specially-designed metallic structures that contain a resonating electric field. This field (tuned to oscillate at 400 MHz, or 400 million times per second) is carefully calibrated such that it boosts the speed of lagging protons, as well as decelerating the particles that are moving too fast. This technology allows the protons to be accelerated to an energy level of 50 MeV (50 mega-electron volts, or 50 million eV) while maintaining them in a tight bunch. Because charged particles experience a force in the presence of magnetic fields, electromagnets are used to control these beams, with dipole magnets (one north and one south pole) used to steer them in the desired direction, and higher-order poles used to focus the beams and make other, subtler adjustments to their structure. Tight (or "intense") beams result in more collisions per bunch crossing, resulting in richer data.

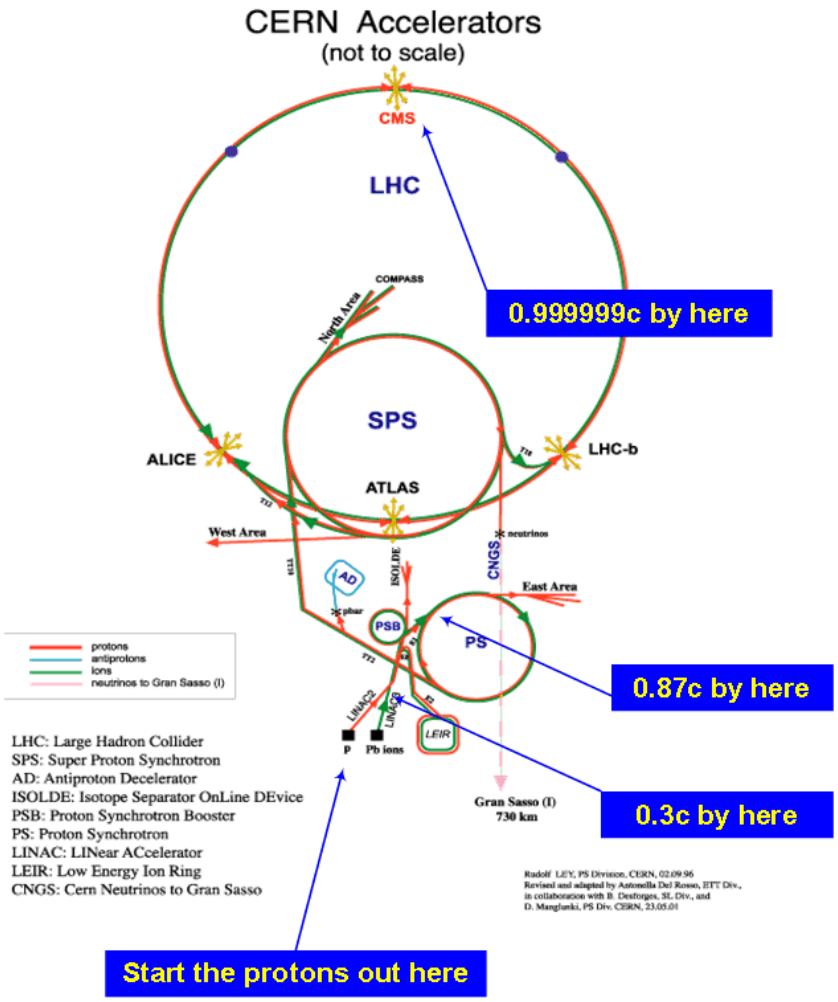


Figure 2.3: The LHC Injector Complex. Protons begin in a linear accelerator, and undergo a series of increases in energy, starting with the Booster (“PSB”), continuing into the Proton Synchrotron (“PS,” right) and proceeding into the Super Proton Synchrotron (“SPS,” center). From there, they are split into two opposing beams and injected into the LHC (top), where they achieve an energy of 6.5 TeV and circulate until they are collided in the detector halls [9].

From the Linac, the proton bunches are guided to the Proton Synchrotron Booster (known simply as the Booster), a circular accelerator that uses the aforementioned RF cavities to pump more energy into the circulating beams before passing them on to the next step. This process is repeated twice more in the progressively larger Proton Synchrotron (PS) and Super Proton Synchrotron (SPS). Finally, the beam exits the SPS

and is split, with one half being injected into the LHC's clockwise tunnel and the other half into the counterclockwise tunnel (Figure 2.3). The LHC's RF cavities perform the final energy boost up to 6.5 TeV per proton, falling short of the speed of light by an ambulatory 3 meters per second. However, due to relativistic effects, this gap in speed represents a literally infinite jump in energy for the protons, which, unlike light itself, have to deal with the asymptotic effects of Einstein's gamma factor on their non-zero mass [6, 8, 9].

Once inside the LHC rings, a proton bunch orbits the 27-km circumference at a rate of over 11,000 times per second until induced to cross with a bunch traveling in the opposite direction. Although the average bunch consists of over 100 billion protons packed into a cross-sectional area roughly that of a human hair, only about 20 actual collisions occur during a given bunch crossing. Thus, each bunch can continue to circulate and cause collisions for hours after being generated. The bunches are spaced 25 nanoseconds (ns) apart, with some larger gaps, giving a peak collision rate of roughly 600 million collisions per second.

### *2.2.2 Proton Collisions*

When two protons collide head-on, their large combined kinetic energy is put into trying to dissociate their component quarks and gluons. The energy densities involved are so large, in fact, that new particles are created from the available energy (as per $E = mc^2$), most of them the constituent particles of the Standard Model (see Chapter 1). Some particles may decay and/or combine with others in what is known as a "channel." Many of the initial products of the collisions are quarks, which quickly combine with one

another via the strong force to form a shower of hadrons. Many are force carriers, such as photons, which carry energy outward in the form of light, and W and Z bosons, which are unstable and decay to less-massive products almost immediately. Also abundant are leptons; of these, many are the ghostly neutrinos, which cannot be reliably observed by general-purpose detectors such as CMS. As a result, some of the total collision energy is lost to these particles, which escape the detector volume without leaving a signal. However, advanced detector systems such as those at the LHC devote significant computing power to the task of reconstructing collisions, and thus analysts are able to identify so-called "invisible" neutrino decay channels with a high degree of accuracy by looking for conspicuous imbalances in the total momentum of a reconstructed event.

Other leptons are produced as well, including electrons, as well as the massive tau, which rapidly decays to a number of less-massive particles, and the muon, which is also unstable but often does not decay until it is outside the detector volume [6].

### *2.3 Overview of the Compact Muon Solenoid*

The Compact Muon Solenoid (CMS) is a large cylindrical detector housed underground in the path of the LHC beamline near Cessy, France. It takes its name from the 3.8-Tesla magnetic field that is projected lengthwise through the detector volume; this field causes charged particles moving away from the beamline to curve, allowing their charge and momentum to be more easily reconstructed from their path. The "Muon" portion of the name comes from the detector's outermost layer, the muon chambers, which help pick up the signature of said particles, as these tend to interact only weakly with the other detector components on their way outward from the beamline.

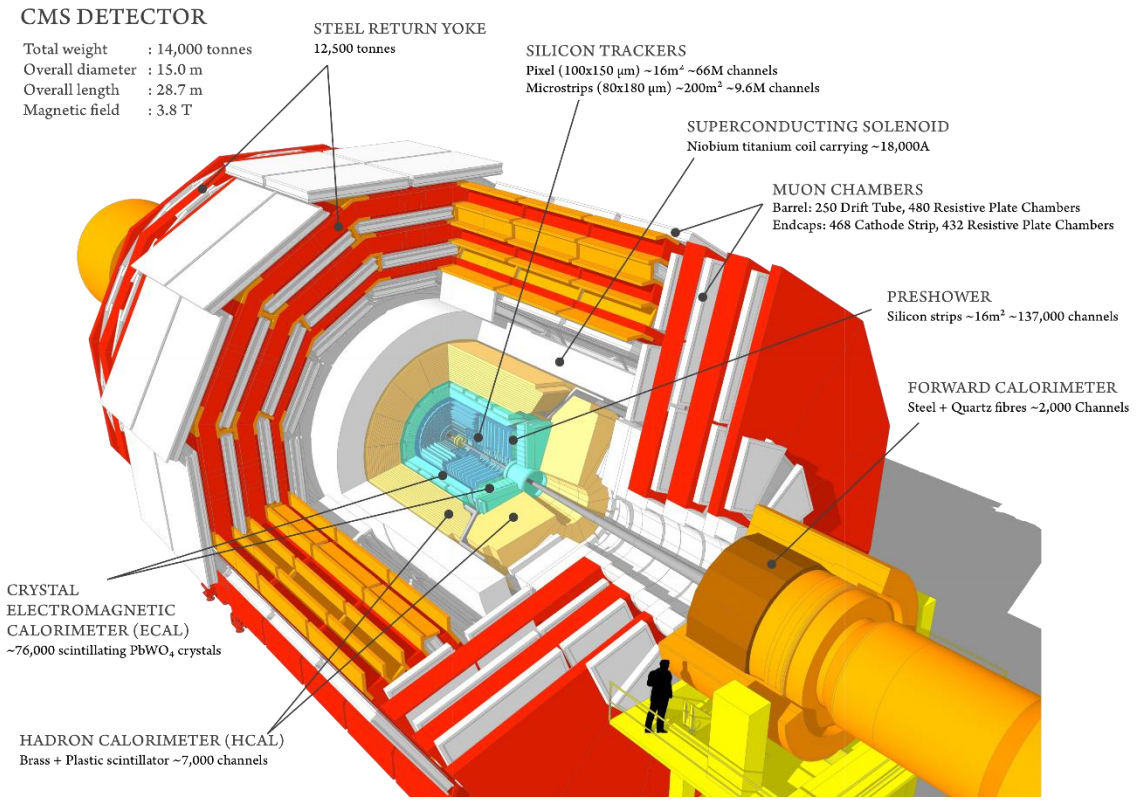


Figure 2.4: A diagram of the Compact Muon Solenoid. The beamline runs through the center of the cylindrical volume, and the subdetectors surround it in concentric layers. Note the Hadron Calorimeter, highlighted in yellow near the central detector area [10].

CMS is designed to fit around the beamline in a series of concentric cylindrical shells, each of which serves a different purpose in the reconstruction of particles. These shells are known as "subdetectors" (Figure 2.4) The closest subdetector to the beamline is called the silicon tracker, which is used to provide information about the charged momenta of particles produced in collisions. The next layer is called the Electromagnetic Calorimeter (ECAL), designed to detect electromagnetic particles, including photons and electrons. Outside the ECAL is the Hadron Calorimeter (HCAL), which detects hadrons, particles made of combinations of quarks bound by the strong force (see Chapter 1). Outside the HCAL is the solenoid from which CMS takes its name, a superconducting

coil that produces the detector's useful magnetic field. The outermost layer is the aforementioned muon chambers, which are used in conjunction with information from the tracker to reconstruct muon paths. This thesis is concerned with the HCAL subdetector.

### *2.3.1 The CMS Hadron Calorimeter*

The HCAL is itself further divided into several different sections: the barrel (HB), which comprises the "walls" of the cylinder, the endcap (HE), the two ends, the forward regions (HF), which are further along the beamline and detect particles leaving at very shallow angles, and the outer region (HO), which lies outside the solenoid.

The HCAL is what is known as a sampling calorimeter. It is composed of many alternating layers of metal and scintillator; the metal (brass in HB and HE, iron in HF) interacts strongly with hadrons, causing them to break into easily detectable "showers" of secondary particles, while the scintillator tiles turn the energy of these passing secondary charged particles into light. This light is guided by wavelength-shifting fibers (WLS) to photodetectors, which turn the light energy into electrical current. This current is then turned into a digital signal and serialized by the front-end electronics, which then relay it to the back-end electronics (see Chapter 3) [11].

## *2.4 The CMS Upgrade*

In order to push physics knowledge as far as possible, the LHC and its detectors are periodically stopped to undergo upgrades to improve their capabilities and efficiency. One such stop, known as Long Shutdown 1 (LS1), lasted from 2013 to 2015, during

which time the energy of the LHC proton beams was increased from 8 TeV to 13 TeV. The latest upgrade, known as Phase 1, is currently being conducted and will continue for several years; during this time, the CMS detector will undergo a concurrent series of upgrades, in order both to stay abreast of the upgraded LHC output and to keep the detector functioning. One of the primary concerns for the upgrade is irradiation of the scintillator tiles and front-end electronics. When exposed to large amounts of radiation over a long period of time, scintillator tiles will become damaged and darken, significantly reducing the amount of light produced by striking particles. The interior of the CMS detector is, necessarily, a radiation-intensive environment due to the particles produced by the colliding proton beams; as a result, it has been observed that light yield from the tiles has been steadily decreasing over the period of CMS's operation. There are methods that can be used to compensate for this; the detector has an internal monitoring system, and analyses of the data produced by the detector can reveal darkening trends which can be taken into account during event reconstruction. However, the ability of the current generation of light-sensing devices, Hybrid Photodiodes (HPDs), is limited by its gain (charge produced per light). Because of this, the CMS collaboration sought new options for photodetection to be installed during the upcoming upgrade.

### *2.4.1 Silicon Photomultipliers*

Silicon photomultipliers (SiPMs) are a promising technology that offers a number of advantages over HPDs in the context of CMS. They are an application of avalanche photodiodes (APDs); in such devices, light causes the emission of an electron, which is subjected to a strong electric field, causing it to gain kinetic energy and trigger more

electrons to be emitted as it moves. This leads to the titular “avalanche” effect. SiPMs are composed of many small APDs that augment one another’s effects, allowing them to detect even single photons with great efficiency. As a result of this design, they have a gain that is roughly 100 times that of the currently-installed HPDs. This gain is linked to their large dynamic range, a measure of the difference in output from low-energy signals to high energy signals. The large dynamic range exhibited by these devices allows unprecedented energy resolution, facilitating particle data analysis. In addition, SiPMs are highly resistant to magnetic fields and radiation, both of which are prominent effects within CMS. Other advantages over HPDs include a lower cost and a much smaller size (about 3 x 3 mm), allowing more of them to be used in the detector (Figure 2.5) [12].

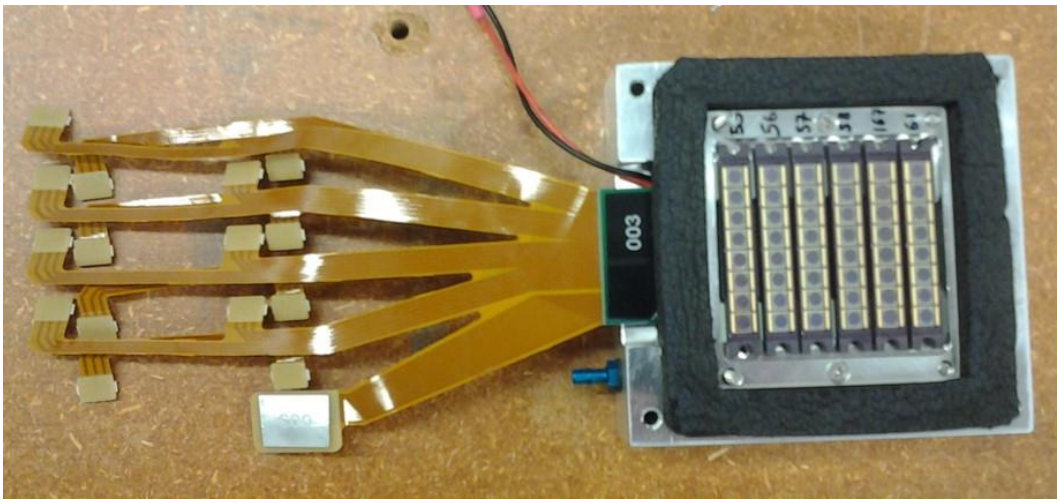


Figure 2.5: A set of 48 SiPMs (right) inside an opened housing cap. Light from the scintillator tiles is guided by fiber-optic cables to the SiPMs. The analog electrical signal that they produce is then sent via the wires on the left to the front-end electronics for digitalization and serialization.

*2.4.2 Depth Segmentation*

Because of the increased number and efficiency of the silicon photomultipliers, the upgrade will make it possible to allocate more photosensors to the tiles, as opposed to the current configuration, which combines the light from many tile layers to feed into each HPD. This improved segmentation will greatly improve tracking and time resolution in the CMS results (Figure 2.6) [11].

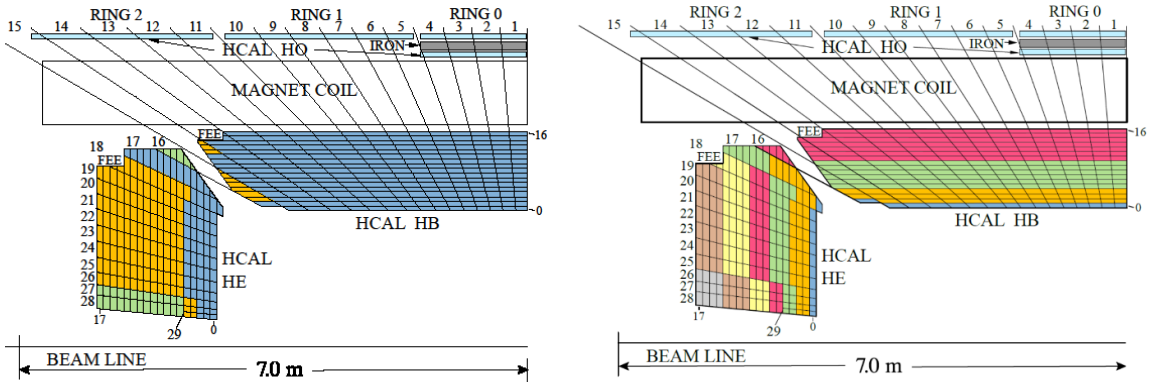


Figure 2.6: The current (left) and planned (right) depth segmentation schemes of a section of the HCAL subdetector [13, 14].

*2.4.3 Front-End Electronics*

After the light from the scintillators is turned into an analog signal by the SiPMs, it must then be changed to a digital format in order for it to be sent to the back-end. This is accomplished by Charge Integrator and Encoder chips (QIEs), which add up the charge received over a short period of time (integration), store it in a system of capacitors, and output a signal that corresponds to the charge received (Analog-Digital Conversion, or ADC) as well as its timing information (Time-Digital Conversion, or TDC). The current detector configuration uses model 8 (QIE8), but plans are being made to replace them with model 11 (QIE11), a later version that improves upon the model 8 in numerous ways,

including a “shunt” system to control the amount of charge received, which allows an increase in sensitivity.

In order to test this configuration in a realistic detector environment, the CMS collaboration conducted a comprehensive test of the proposed upgraded system. This test is the subject of subsequent chapters.

# CHAPTER THREE

# Apparatus and Method: The 2015 HCAL Test Beam

## *3.1 Test Beam Overview*

### *3.1.1 Test Beam Concept*

In order to characterize systems designed to detect high energy particles, a source of such particles is needed. It is often desirable to have a fine degree of control over the particles to which the detector system is exposed in order to evaluate the performance of the detector system. To this end, CERN has created a number of areas in which proton beams from smaller LHC-feeding accelerators, like the Super Proton Synchrotron (SPS), can be diverted from the LHC and used to create beams of other particles that can be aimed at specialized targets. Such an experimental setup is usually referred to as a test beam facility. Test beam times are tightly scheduled to ensure that the LHC can maintain its own beam as efficiently as possible.

In late summer 2015, a number of members of the CMS collaboration met at the CERN site for the purpose of conducting a full integration test of the proposed upgraded HCAL electronics configuration. This involved constructing a working prototype of the upgraded front-end and back-end electronics, which had been extensively tested and characterized in the preceding months by a team at Fermi National Accelerator Laboratory (FNAL), including members of Baylor University's High Energy Physics research group. In order to gain a comprehensive understanding of the behavior of the

full system, it was deemed necessary to test it in as realistic an environment as possible. Thus, the set of pre-vetted prototype electronics was then shipped in late July to CERN headquarters in Geneva, Switzerland, in order to be installed for a scheduled test beam from the end of July to mid-August.

### *3.1.2 The H2 Test Beam Facility*

Our tests were conducted at the CERN H2 Test Beam Facility, a long, enclosed structure designed to allow special particle beams to travel down its length (Figure 3.1).

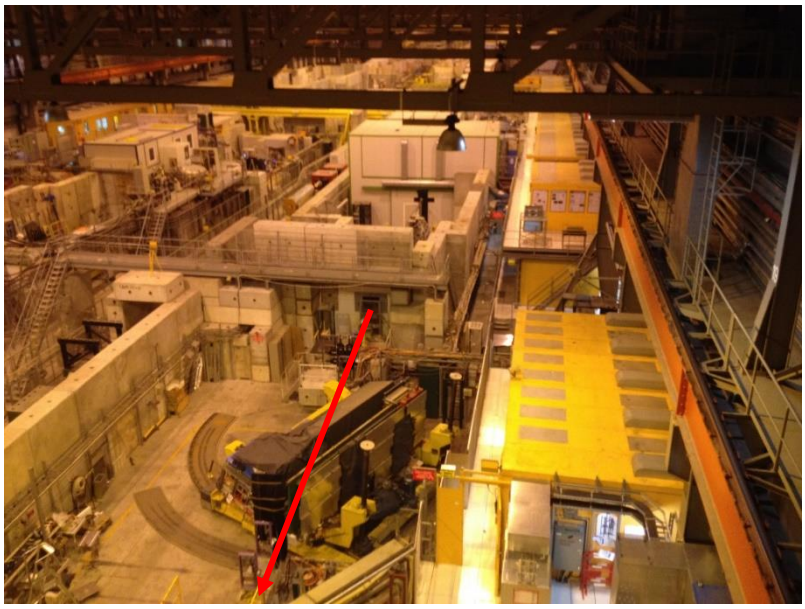

Figure 3.1: A high-angle view of the HCAL translation table apparatus (foreground) inside the H2 Test Beam Facility. The beam that we used for our tests was fired down the length of the building in the direction indicated by the arrow. Because the beam emerged from a stationary source, multiple experimental enclosures were placed in its path.

In order to create these beams, protons from the SPS accelerator are collided with targets to produce showers of particles (mostly electrons, hadrons, and muons), which are then guided and filtered using a configurable set of magnets and beam absorbing materials [15].

This system makes it possible to specify the approximate fraction of each type of desired particle appearing in the beam. For the purposes of our tests, we almost exclusively used either pions (a type of hadron) or muons. Each of these served an important purpose: muons are minimum ionizing particles (MIPs), charged particles which embody the minimum ionizing losses in substances such as scintillator. Because of this property, they tend to produce a clear signal to all layers of scintillators, allowing us to analyze how the system responds to different particle energies, whereas pions, being hadronic, are a good test of the detector's response to the type of signal for which it is intended.


Figure 3.2: The HCAL translation table apparatus at the H2 Test Beam Facility. The beam path is highlighted in white. Also highlighted are the two sections of the detector, HCAL Barrel (HB) and HCAL Endcap (HE).

The electronics were mounted on the HCAL translation table, which contains a full-scale model of a portion of the HCAL, comprising a radial "slice" of approximately 20° of half of the barrel length (Figure 3.2). Like the HCAL itself, the model mounted on the translation table consists of interleaved layers of brass and scintillator material, and it is designed to simulate the light output of the barrel and endcap portions of HCAL (HB and HE, respectively). As the name might suggest, the translation table is able to rotate in 2 dimensions (η [Greek letter eta], a coordinate corresponding to the angle between a particle path and the z-axis of the detector, and φ [Greek letter phi], representing the angle of a particle path within the circular detector cross-section (Figure 3.3). Also used are the two corresponding measures ieta and iphi, which are indices for individual eta and phi segmentation of the HCAL. In the testing apparatus, because the beamline is fixed, the translation table is designed to rotate with the aid of electric motors to allow beam to be incident on a particular η-φ coordinate.

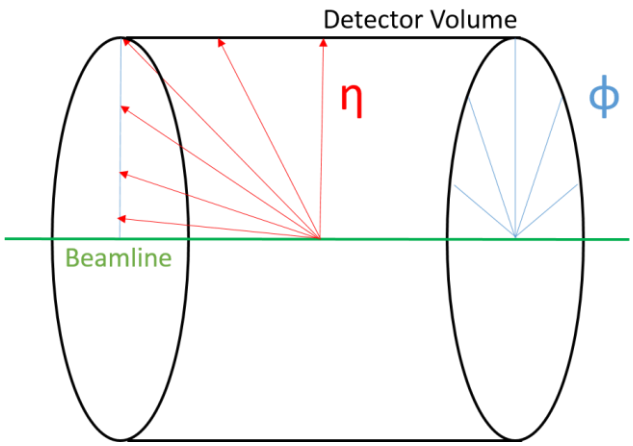


Figure 3.3: Diagram of eta and phi as used by CMS. Higher eta values lie more parallel to the beamline, while phi describes the azimuthal angle about the beamline.

The output produced by the scintillator tiles in the table-mounted apparatus is, as in HCAL, read out by fiber-optic cables. In the testing apparatus, the area in which the

readout electronics are mounted is designed for relatively easy access, allowing different configurations to be attached directly to the scintillator output.

### *3.1.3 Electronics*

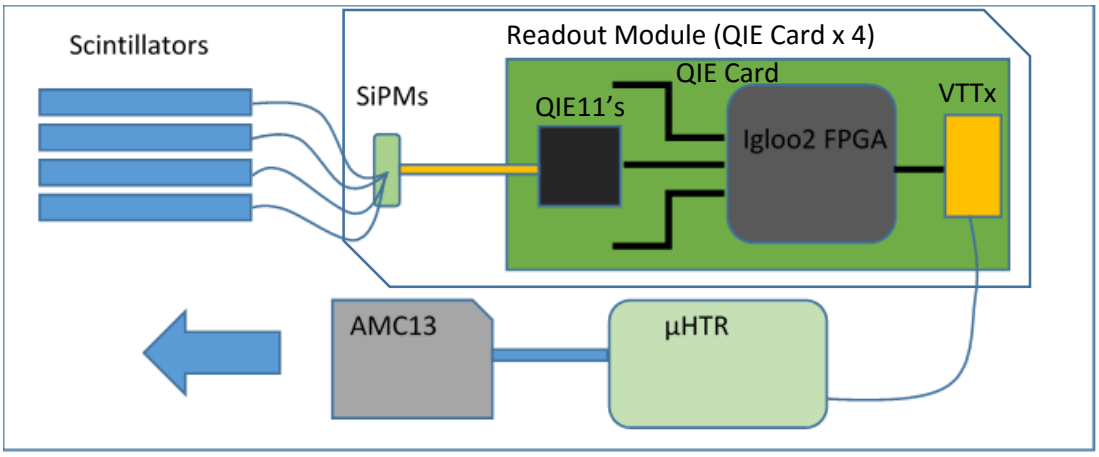


Figure 3.4: A diagram of the front-end electronics. Light from the scintillators is collected by the SiPMs, which send an electrical signal to the QIE chips. The resulting digital signal is serialized by the Igloo FPGA and sent to the back-end by the VTTx optical transmitters through a fiber-optic cable.

The majority of front-end components are contained in Readout Modules (RMs), which turn the analog light signal from the fiber-optic cables into a digital representation of light intensity (Analog-Digital Conversion or ADC) and timing information (Time-Digital Conversion, or TDC). The RM is a major step in the information flow of HCAL (see Figure 3.4). Each upgrade RM processes signals from 48 channels. There are four RMs in one Readout Box (RBX), along with a Calibration Module (CM), used for injecting test signals into the RMs from an LED source, and a next-generation Clock and Control Module (ngCCM), which monitors the status of the RMs and mediates the optical link to the back-end electronics.

The optical output from each RBX comes in the form of a 40 MHz signal from a Versatile Twin Transmitter (VTTx). This is carried by fiber-optic link to the Data-Acquisition system, or DAQ. Timing between the system components is mediated by a 40 MHz "trigger" signal that, in the actual detector, is designed to coincide with the crossing of two proton bunches in the detector hall. In our testing configuration, we triggered the system using beam detector tiles located in the beam path.

### *3.2 Configuration*

For the purposes of the test beam, six full prototype Readout Modules were constructed at FNAL, as well as an ngCCM emulator and a CM. Four of these components were placed in an RBX housing and used to read out a section of the table-mounted HCAL apparatus corresponding to 10° of detector wedge. For comparison purposes, another RBX was read out from a neighboring region using the current electronics configuration and HPDs. In addition, scintillator materials for the Phase 2 upgrade were mounted on the reverse side of the table from the beam (Figure 3.5).

The optical links from the front-end were carried by a system of fiber-optic cables to the back-end. For the purposes of the test, the back-end electronics were located in an office area overlooking the test beam enclosure, which was locked when beam was on. To take data, we used a scheduling system on the CERN computer network to request a beam configuration, then set the DAQ to record data for a specified number of triggers, usually 5,000-10,000 but sometimes up to 100,000. The data were passed to an on-site computer in the CMS common data format, and stored in one of several servers located alongside the DAQ electronics.

We used beams of muons with a momentum of 150 GeV each to calibrate the translation table alignment and relative energy calibration of our readout system, and pion beams at a range of energies to test the system's response to hadronic signals.

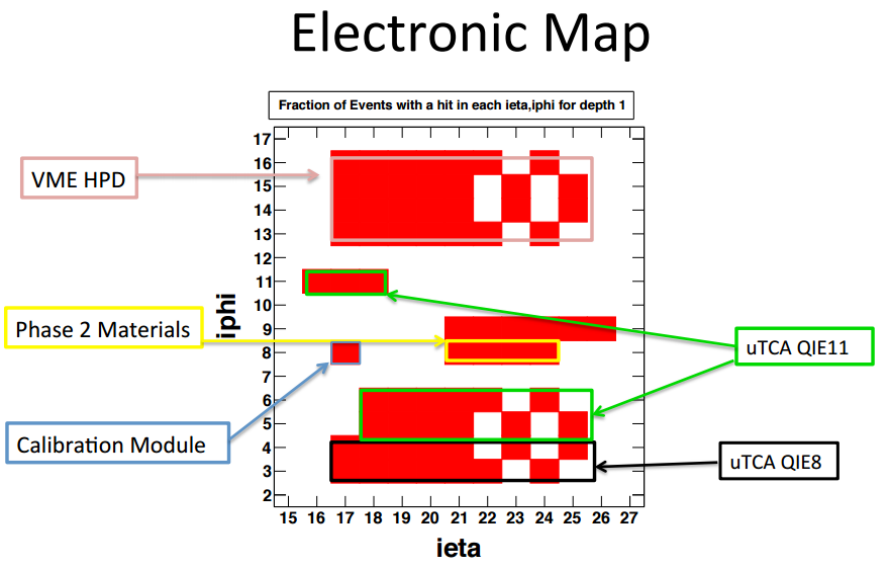


Figure 3.5: A map of the electronic components at the test beam in eta-phi coordinates. The section from iphi = 13 to iphi = 16, named thus for convenience, corresponds to an alternate readout of the same front-end signal (actual coordinates iphi = 3 to iphi = 6, as in the lower section). The black-highlighted area was our reference readout, consisting of the electronics chain currently used by CMS. Note the presence of the Phase 2 materials, indexed at iphi = 8 to iphi = 9 for convenience but actually located at roughly iphi = 5.

# CHAPTER FOUR

## Results and Conclusions

### *4.1 Energy Spectra*

The energy spectrum of a detector system is a histogram of its response to a given stimulus. A major concern of the testers was to establish that the quality of data produced by SiPMs was comparable, if not superior, to that of HPDs. To that end, we plotted the energy spectra of SiPMs and HPDs for the same type of input. We were able to identify numerous features of the various spectra produced, some of which were due to the beam, and some of which were artifacts of the photodetectors. We chose to use 150 GeV muon beams. As stated earlier, muons leave a clean signal of minimum ionizing energy in each layer of scintillator. We were then able to compare the dynamic range and energy resolution of the devices against one another.

Qualitative inspection of these plots (see Figure 4.1) reveals that the SiPMs have a number of advantages over the HPDs in operation. Primarily, their dynamic range (distance between zero signal [left peak] and some given energy [for example, the large muon energy peak on the right]) is wider and better-defined than that of the HPDs, as can

be seen by comparing the pedestal location on the SiPM plot, ~$10^{-3}$, to that on the HPD plot, ~$10^{-1}$. This means that the SiPMs have an improved resolution.

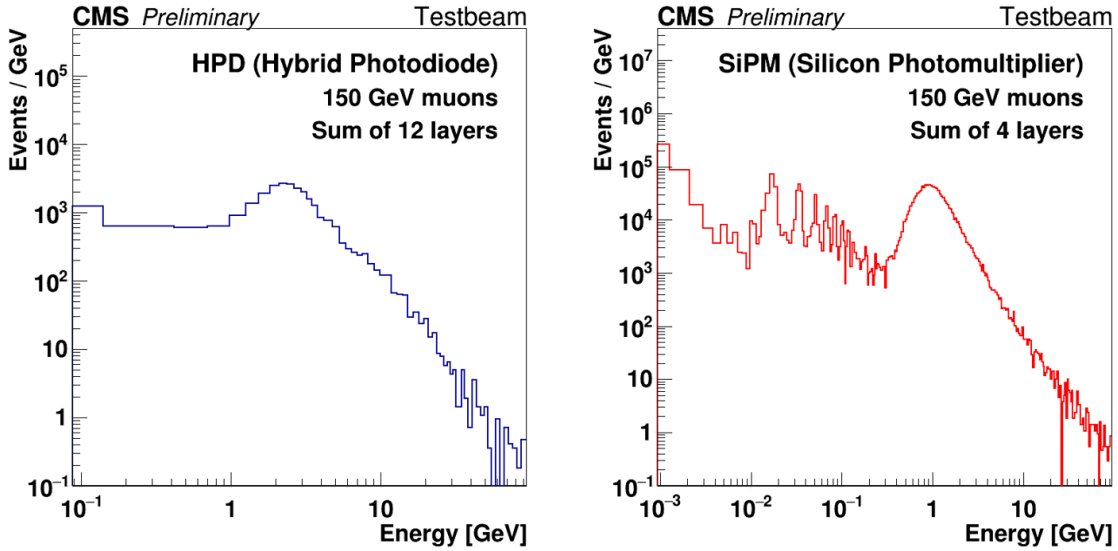


Figure 4.1: Side-by-side comparison of HPD and SiPM response histograms for the same beam type, 150 GeV muons (courtesy of N. J. Pastika). The large peak in each plot is the energy deposited by the muon beam.

A consequence of this is evidenced by the clear visibility in the SiPM plot of the central set of peaks, called the photoelectron peaks (PE peaks). These peaks are the detector's response to individual photons striking it, with the leftmost PE peak (at ~$10^{-2}$) corresponding to a single electron emission due to an incident photon, the next one representing the emission of two electrons, etc. Note that no such features can be distinguished from the HPD spectrum. This is evidence that the SiPMs have a greater resolution, which allows them to report more fine-grained information regarding particle energies.

## *4.2 Gain Calculation*

### *4.2.1 SiPM Gain Using Photoelectron Fits*

Silicon photomultipliers, being sensitive electronic devices, are potentially prone to variations in gain from SiPM to SiPM. That is, for a given number of photons as input, one device may consistently output a larger signal than another by some predictable factor.

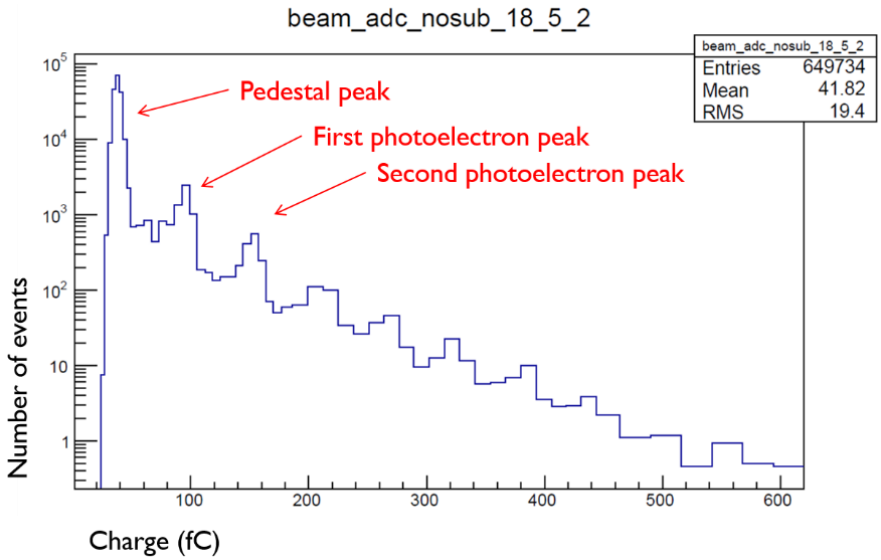


Figure 4.2: A typical charge spectrum at pedestal. Note the regular spacing of the PE peaks.

In a detector such as CMS, if a SiPM connected to one set of scintillator tile had a significantly larger or smaller gain than another, this could manifest itself as a spuriously large or small energy deposition in that area of the detector, which could adversely affect the quality of the data.

In order to gain an understanding of the distribution of relative SiPM gains and correct for differences between different SiPM devices, we devised a method to estimate

the relative gain of SiPM channels given a sample of their pedestal spectrum, the range of ADC values they produced when exposed to voltage but no light signal. To obtain this information we took runs from the DAQ with the SiPMs disconnected from their respective fibers.

The results were of the form shown in Figure 4.2. The peaks shown are the pedestal and PE peaks. PEs produced in the SiPMs are equally amplified in a single device, so the PE peaks should be located at regular intervals. By measuring the relative gain of each SIPM based on the PE peak intervals, we can correct for the gain variation of different SiPMs in reconstruction. This had the effect that the distance between the PE peaks represented a constant charge, meaning that the PE peak spacing for two devices with the same gain should be equal.

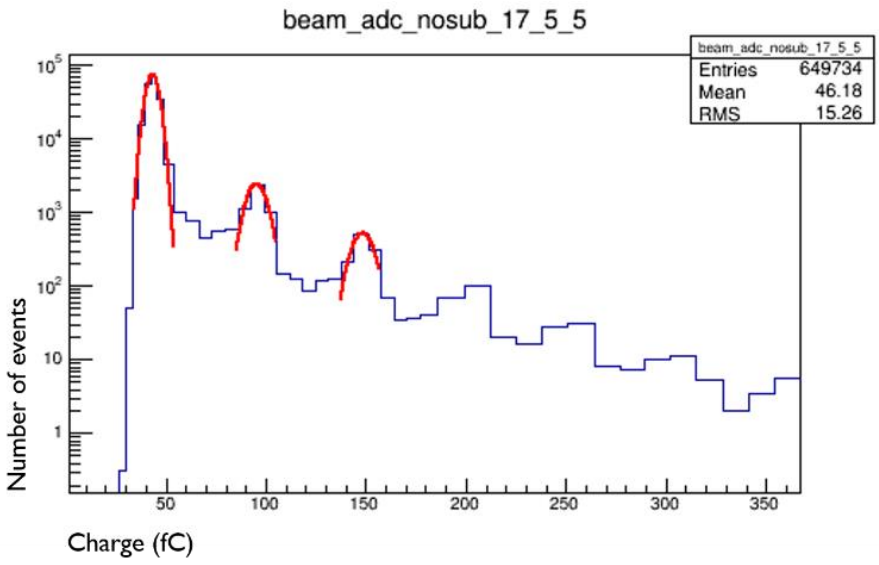


Figure 4.3: Gaussian fits on the first three peaks of a SiPM pedestal spectrum.

We were able to calculate the relative gain levels of the devices using a C++ program to report the location of the first three peaks (see Figure 4.3). The program fit a

Gaussian peak to each and calculated two values: the distance between the pedestal and the first PE peak, and the distance between the first PE peak and the second. It then returned the average of these values as a measure of the channel's gain. The ratio of the gain of two channels could then be approximated as the ratio of this measure.

We created a histogram of the relative gain measures of the set of SiPMs that we were testing in order to find any outliers, which would represent a problem in manufacturing. We found that the histogram of relative gain for our devices followed an approximately normal distribution and was relatively narrow (see Fig. 4.4). No significant outliers were found. This suggests that the manufacturing process for the devices we received was reliable and consistent.

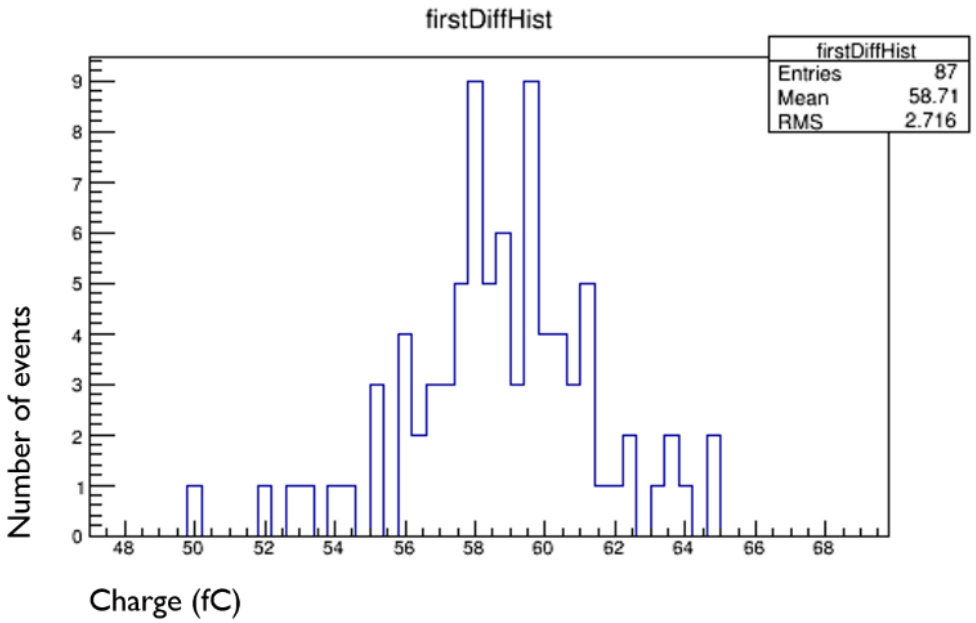


Figure 4.4: Histogram of relative gain values for the SiPMs tested.

The relative gain values, which were used in later analyses to calibrate channel input, were confined to a narrow region, with no values straying lower than 50 or higher that 65, where these values are the approximate charge in femtocoulombs (fC) recorded from the device. We concluded that what differences there were in gain from device to device were predictable and easily corrected and that we could be confident regarding relative signal quality.

### *4.2.2 Gain Using More Advanced Algorithms*

We later created a more advanced model of SiPM response, taking into account the numerous physical processes present in such a device. As opposed to the preliminary fitting function, the later function was continuous, and attempted to fit every feature rather than just the first several peaks. The original code was written in C++ using the ROOT framework by Dr. Nathaniel Pastika, a Baylor postdoctoral researcher, and later changes and function tuning were performed by the author.

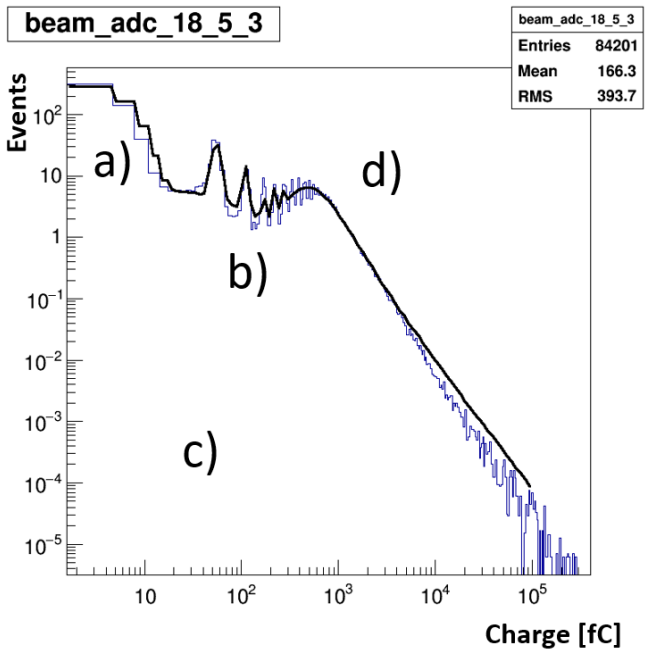


Figure 4.5: An example of a fit (black line) on data from a run of 150 GeV muons (blue line).

The function consists of four major components: a) a Gaussian pedestal, b) several Gaussian photoelectron (PE) peaks, c) a Landau function background contribution, d) a Landau-Gaussian convolution for muon signals (see Figure 4.5) [16]. The Landau function is commonly used to model the spectrum of energy deposited by minimum ionizing particles. The Gaussian is a good general descriptor of smeared signals from detectors, in this case, the spread of pedestal and PE peaks. The Landau-Gaussian convolution refers to the result of convolving the Landau function and a Gaussian, where convolution is defined as, for some input functions *f(x)* and *g(x)*, the operation *(f * g)*, where

$$(f * g)(x) = \int_{-\infty}^{\infty} f(y)g(x-y)dy$$

Thus, we deemed the convolution of a Landau function and a Gaussian function to be a good representation of the output from a detector that was receiving particles as input, as the particles would deposit energy according to the Landau distribution, while the detector would report that energy according to the Gaussian distribution [17]. In order to produce robust fits, the SiPM charge spectrum model required some tuning of starting parameters, and we used Baylor's high-performance computing system, Kodiak, to analyze the output that resulted from fitting our model to the test beam results. We iteratively refined the algorithm and the bounds of its allowed parameter space until it was able to perform robustly in fitting virtually all muon beam histograms.

This process involved iteratively tuning two aspects of the fit function: the function parameter initial values and the parameter bounds. We judged the accuracy of a fit by how it appeared to visually align to the data, the final values of the parameters, and the chi-square value of the comparison between data and model (a measure of how "close" two functions are). This required many repetitions of the modeling process, during which we would change our initial conditions, run the analysis code on a dataset, and inspect the results for fit quality. Because the fitting process was computationally intensive, we used Kodiak to perform much of the analysis. The author wrote a series of scripts for Kodiak's Linux command-line environment to automate a portion of this process, allowing the analysis to be re-run quickly with new parameter settings and uploading the resulting plots to a server for easy viewing.

In addition to creating the fit plots, the aforementioned system also created plots of the value of each of the 13 parameters over every plot, as well as parameter-vs.-parameter correlation plots. The former allowed us to see whether parameter values were

falling naturally within their given range or trying to “escape” to a larger or smaller value, which usually suggested that loosening the bounds would improve the fit. The latter gave us an indication of the degree to which one parameter was associated with another. This was especially relevant in light of the tendency of the fitting software to compensate when a parameter was too tightly bound to reach an accurate value, causing other aspects of the function to increase or decrease to bring the measure of fit accuracy to a minimum.

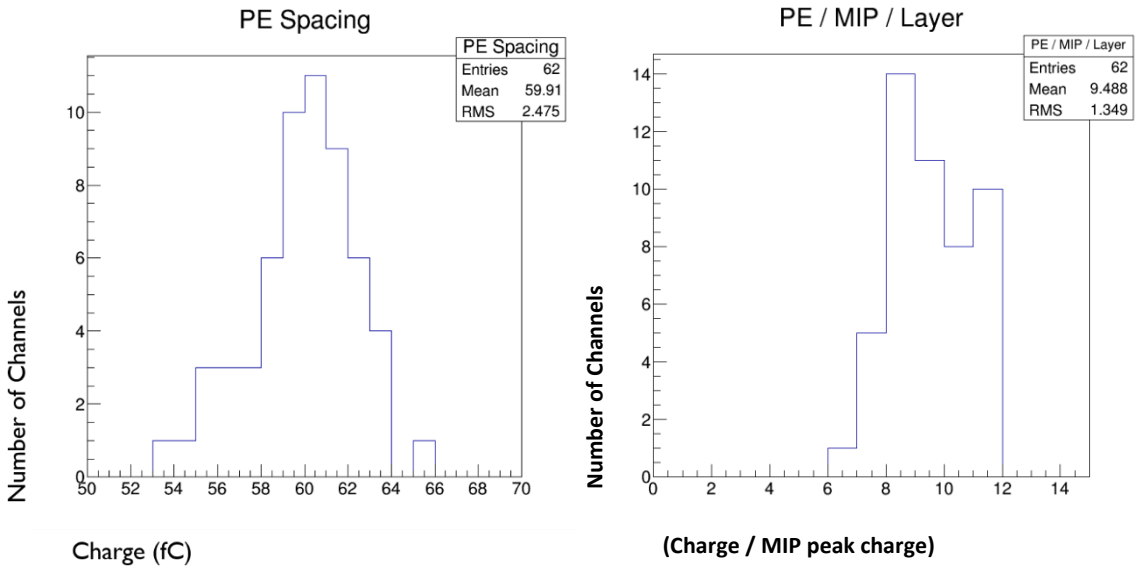


Figure 4.6: (Left) The recalculated distribution of channel gain. Note that the improved data is not only smoother, but slightly better confined as well (See Appendix B). (Right) The distribution of channel PE spacing divided by the muon peak value.

Once tuned, the model allowed much more detailed conclusions to be drawn from our dataset. In particular, we were able to reproduce the histogram of channel gains using this method, resulting in the improved plot shown in Fig. 4.6 (left). We also examined the histogram of the same set of peak spacing values, each divided by the location of the muon peak signal. Because the energy from the muon beams was expected to be constant,

this placed each datum in the context of a single energy scale (Figure 4.6, right). This distribution was also relatively well-confined, and roughly centered about the value 9, giving the result that approximately 9 photoelectrons were emitted for each muon striking the scintillator. These results corroborated our conclusions regarding the SiPM data quality.

### *4.3 Conclusions*

The LHC and its detectors, already one of the most celebrated and ambitious sets of experiments in the world, are in a constant state of improvement, and the upcoming upgrades are no exception. Our work at the 2015 test beam was part of a large-scale effort to improve the performance of the Compact Muon Solenoid's Hadron Calorimeter using new technologies such as silicon photomultipliers and the QIE11 chips. The HCAL 2015 test beam was a success, serving as a full integration test of the upgraded electronics, as well as allowing extensive characterization of the silicon photomultipliers. These devices were found to represent a vast improvement over the currently-installed Hybrid Photodiodes in a number of notable respects, including increased durability, improved gain, and better signal discrimination. The pre-production SiPMs tested demonstrated a relatively narrow range of relative gain, which suggests that the manufacturing process is reliable, and, further, that the energies reported by different sectors of detector were mutually consistent. Overall, the SiPMs used by the testers were found to be reliable and well-suited to the role of CMS Hadron Calorimeter readout electronics.

Most importantly, we successfully assembled and tested a working subsection of the improved HCAL front-end electronics. We were able to construct and maintain a continuous data link from the silicon photomultipliers, through the digitization process in the Readout Modules, to the back-end electronics, and finally to computer-readable files. Moreover, we used our proof-of-concept system to capture and analyze data from well-understood particle sources, comparing them with expected results and finding the performance satisfactory. The system as it stands has been demonstrated to be viable, and as such, much of it will be incorporated into the upcoming improved CMS detector. When the upgrade is completed, we expect that CMS will enjoy not only an extended lifetime, but improved data quality.

# APPENDICES

# APPENDIX A

## C++ Code Sample: Landau-Gaussian Convolution Function

```
// landau-gaussian convolution using numerical integration
Double_t langaufun(Double_t *x, Double_t *par) {
    //Fit parameters:
    //par[0]=Width (scale) parameter of Landau density
    //par[1]=Most Probable (MP, location) parameter of Landau density
    //par[2]=Total area (integral -inf to inf, normalization constant)
    //par[3]=Width (sigma) of convoluted Gaussian function
    //In the Landau distribution (represented by the CERNLIB approximation),
    //the maximum is located at x=-0.22278298 with the location parameter=0.
    //This shift is corrected within this function, so that the actual
    //maximum is identical to the MP parameter.

        // Numeric constants
        const Double_t invsq2pi = 0.3989422804014;   // (2 pi)^(-1/2)
        const Double_t mpshift  = -0.22278298;       // Landau maximum location

        // Control constants
        const Double_t np = 100.0;      // number of convolution steps
        const Double_t sc =   5.0;      // convolution extends to +-sc Gaussian sigmas

        // Variables
        Double_t xx;
        Double_t mpc;
        Double_t fland;
        Double_t sum = 0.0;
        Double_t xlow,xupp;
        Double_t step;
        Double_t i;

        // MP shift correction
        mpc = par[1] - mpshift * par[0];

        // Range of convolution integral
        xlow = x[0] - sc * par[3];
        xupp = x[0] + sc * par[3];
        step = (xupp-xlow) / np;

        // Convolution integral of Landau and Gaussian by sum
        for(i=1.0; i<=np/2; i++) {
            xx = xlow + (i-.5) * step;
            fland = TMath::Landau(xx,mpc,par[0]) / par[0];
```

```
            sum += fland * TMath::Gaus(x[0],xx,par[3]);
            xx = xupp - (i-.5) * step;
            fland = TMath::Landau(xx,mpc,par[0]) / par[0];
            sum += fland * TMath::Gaus(x[0],xx,par[3]);
        }
        return (par[2] * step * sum * invsq2pi / par[3]);
}
```

APPENDIX B

SiPM Gain Values by Channel

| Eta | Phi | Depth | Gain |
|---|---|---|---|
| 16 | 6 | 2 | 58.66 |
| 16 | 6 | 3 | 57.771 |
| 17 | 5 | 2 | 62.26 |
| 17 | 5 | 3 | 60.10 |
| 17 | 5 | 4 | 60.45 |
| 17 | 5 | 5 | 63.35 |
| 17 | 5 | 6 | 59.27 |
| 17 | 5 | 7 | 74.70 |
| 17 | 5 | 8 | 74.05 |
| 17 | 5 | 9 | 60.15 |
| 17 | 5 | 10 | 55.40 |
| 17 | 5 | 11 | 60.21 |
| 17 | 5 | 12 | 75.32 |
| 17 | 5 | 13 | 61.22 |
| 17 | 6 | 2 | 56.27 |
| 17 | 6 | 3 | 63.14 |
| 17 | 6 | 4 | 57.75 |
| 17 | 6 | 5 | 59.42 |
| 18 | 5 | 1 | 53.37 |
| 18 | 5 | 2 | 58.50 |
| 18 | 5 | 3 | 55.28 |
| 18 | 5 | 4 | 61.92 |

| | | | |
|---|---|---|---|
| 18 | 5 | 5 | 65.80 |
| 18 | 5 | 6 | 60.13 |
| 18 | 5 | 7 | 59.01 |
| 18 | 5 | 8 | 59.82 |
| 18 | 5 | 9 | 58.77 |
| 18 | 5 | 10 | 55.31 |
| 18 | 5 | 11 | 59.62 |
| 18 | 5 | 12 | 59.37 |
| 18 | 5 | 13 | 62.94 |
| 18 | 5 | 14 | 60.43 |
| 18 | 5 | 15 | 60.57 |
| 18 | 5 | 16 | 60.09 |
| 18 | 6 | 1 | 61.74 |
| 18 | 6 | 2 | 56.21 |
| 18 | 6 | 3 | 61.46 |
| 18 | 6 | 4 | 57.90 |
| 18 | 6 | 5 | 61.95 |
| 18 | 6 | 6 | 60.69 |
| 19 | 5 | 1 | 58.64 |
| 19 | 5 | 2 | 59.50 |
| 19 | 5 | 3 | 56.28 |
| 19 | 5 | 4 | 59.85 |
| 19 | 5 | 5 | 59.24 |
| 19 | 5 | 6 | 58.71 |
| 19 | 5 | 7 | 76.88 |
| 19 | 5 | 8 | 58.36 |
| 19 | 5 | 9 | 61.55 |

| | | | |
|---|---|---|---|
| 19 | 5 | 10 | 54.61 |
| 19 | 5 | 11 | 61.45 |
| 19 | 5 | 12 | 61.17 |
| 19 | 5 | 13 | 60.24 |
| 19 | 5 | 14 | 62.32 |
| 19 | 5 | 15 | 61.50 |
| 19 | 5 | 16 | 63.72 |
| 19 | 5 | 17 | 62.85 |
| 19 | 6 | 1 | 63.69 |
| 19 | 6 | 2 | 60.25 |
| 19 | 6 | 3 | 62.54 |
| 19 | 6 | 4 | 62.33 |
| 19 | 6 | 6 | 59.28 |

# BIBLIOGRAPHY


[1] “History of Particle Physics.” The Particle Adventure. Lawrence Berkeley National Laboratory, n.d. Web.

[2] Kullander, Sven. “Accelerators and Nobel Laureates.” Accelerators and Nobel Laureates. Royal Swedish Academy of Sciences, n.d. Web.

[3] “Long Shutdown 1.” CERN Timelines. CERN, n.d. Web.

[4] Butterworth, Jon. "The Standard Model: How Far Can It Go and How Can We Tell?" ArXiv. Cornell University Library, 12 Jan. 2016. Web.

[5] Hamilton, Andrew. "Special Relativity." Special Relativity. Center for Astrophysics and Space Astronomy, 14 Oct. 2002. Web.

[6] CERN. "LHC Collisions." LHC Collisions. CERN, n.d. Web.

[7] "A Cut-away View of the LHC." Department of Physics & Astronomy. Iowa State University, n.d. Web.

[8] CERN. "CERN Accelerating Science." The Large Hadron Collider. CERN, n.d. Web.

[9] "LHC Images." LHC Images. CERN, n.d. Web.

[10] Taylor, Lucas. "Sectional View of the CMS Detector." CMS Detector Design. CMS Experiment, 23 Nov. 2011. Web.

[11] "Hadron Calorimeter." Hadron Calorimeter. CMS Experiment, 23 Nov. 2011. Web.

[12] Freeman, Jim. "Silicon Photomultipliers for the CMS Hadron Calorimeter." ResearchGate. Fermi National Accelerator Laboratory, May 2010. Web.

[13] CMS Collaboration. "Performance of CMS Hadron Calorimeter Timing and Synchronization Using Test Beam, Cosmic Ray, and LHC Beam Data." INSPIRE-HEP. CMS Collaboration, 2010. Web.

[14] Chlebana, Frank, and David Lange. "USSTF - Status." UPO Meeting (n.d.): n. pag. CERN Indico. CMS Experiment, 1 Nov. 2013. Web.

[15] CERN Engineering Department. "How to Control the North Area Beam Lines." Secondary Beams & Areas. CERN, 2012. Web.

[16] Gallego, L., J. Rosado, F. Blanco, and F. Arqueros. "Modeling Crosstalk in Silicon Photomultipliers." J. Inst. Journal of Instrumentation 8.05 (2013): n. pag. ArXiv. Departamento De Fısica Atomica, Molecular Y Nuclear, Universidad Complutense De Madrid, 6 Feb. 2013. Web.

[17] Weissstein, Eric W. "Convolution." MathWorld. Wolfram Alpha, n.d. Web.